Defining deep-subwavelength-resolution, wide-color-gamut and large-viewing-angle flexible subtractive colors with an ultrathin asymmetric Fabry-Perot lossy cavity

Jiancun Zhao[#], Meng Qiu[#], Xiaochang Yu, Xiaoming Yang, Wei Jin, Dangyuan Lei[*], Yiting Yu[*]

Dr. J. C. Zhao, Dr. X. C. Yu, X. M. Yang, Prof. Y. T. Yu
Key Laboratory of Micro/Nano Systems for Aerospace (Ministry of Education)
Shaanxi Province Key Laboratory of Micro and Nano Electro-Mechanical Systems
Northwestern Polytechnical University
Xi'an 710072, China
E-mail: yyt@nwpu.edu.cn
Dr. M. Qiu, Prof. W. Jin
Department of Electrical Engineering
The Hong Kong Polytechnic University
Hong Kong 999077, China
Dr. D. Y. Lei
Department of Materials Science and Engineering
City University of Hong Kong
Hong Kong 999077, China
E-mail: dangylei@cityu.edu.hk
[#]Dr. J. C. Zhao and Dr. M. Qiu contributed equally to this work.

Keywords: structural color, wide color gamut, large viewing angle, high resolution, flexible optoelectronics

Abstract: Achieving structural colors with wide color gamut, large viewing angle and high resolution remains practically challenging. Here, we propose an asymmetric Fabry-Perot (F-P) lossy cavity to realize subtractive colors, simultaneously featuring wide gamut, angle insensitivity, high resolution and good flexibility. Our experimental results demonstrate that the realized structural colors are insensitive to the viewing angle up to ±60º, arising from the negligible light propagation phase shift in the ultrathin lossy cavity made of an amorphous silicon (*a*-Si) layer; they also exhibit a wide color gamut covering the whole CMY color system, simply achieved through changing the thicknesses of the top metal layer and the middle lossy *a*-Si layer. The ultrathin configuration enables printing such colors at a deep-subwavelength resolution, and the ease of experimental fabrication enables their implementation on soft substrates. Accordingly, a two-dimensional sketched image is printed

using this cavity at a resolution of 150,000 dots per inch (dpi) in the geometrical space, corresponding to a minimum color pixel of 160 nm, well beyond the diffraction limit; a flexible structural color membrane with wide color gamut and large viewing angle is well adhered on an airplane model with a complex surface profile. These new intrinsic properties and functionalities of our F-P-cavity-based structural colors significantly extend its potential to the fields of flexible optoelectronics and purposely counterfeiting, not limited to high-definition displays and optical filtering devices.

1. Introduction

Generally, the colors in nature can be divided into two categories: physical structural color and chemical absorptive color. Traditional chemical color comprising dyes or pigments cannot stand long-time illumination, and usually results in severe environmental pollution. In comparison, the physical structural color has been widely studied owing to its distinct merits, e.g. performance durability, radiation resistance, and being environmentally friendly. Therefore, structural color has gained a great deal of interest in recent years due to its wide range of applications, e.g. color decoration, display, imaging, sensing, printing, among many others.[1-3]

For the applications of structural color, wide color gamut, large viewing angle, high resolution, good flexibility and scalable fabrication are the major issues to be addressed. Since the discovery of the extraordinary optical transmission (EOT) phenomenon,[4] many kinds of structural colors have been demonstrated with a variety of plasmonic nanostructures, such as periodic subwavelength nanoholes,[5-10] metallic nanodisk arrays,[11-15] hybrid nanohole-nanodisk structures,[16-20] metallic nanoparticles[21,22] and subwavelength metallic gratings.[23-25] In general, the structural colors achieved by the aforementioned plasmonic nanostructures highly depend on the pre-defined stringent geometrical and structural parameters, the realization of which all relies on complicated multi-step fabrication processes, such as

nanoimprint lithography, electron-beam lithography, reactive ion etching, and focused ion beam milling, etc. These demanding techniques result in very high fabrication cost and thus drastically limit the large-area implementation of plasmonic structural colors in real-world circumstances. Therefore, realizing structural colors on a large scale with significantly simplified configurations of micro- or nanostructures represents a great challenge in the field of micro- and nanophotonics.

In fact, structural colors in the form of multilayer structures widely exist in nature, e.g. insects, fishes, plant leaves and algae, the colorful skins or surfaces of which are all made of multilayers.[26,27] A typical multilayer-based structural color is the Fabry-Perot (F-P)-type cavity, comprising two metallic mirrors separated by an optically transparent dielectric spacer, where the generation of structural colors is originated from the interference between multiple reflected light beams within the cavity.[28-32] Although conventional F-P-type cavities-based structural colors are relatively easy to realize in experiment, they are sensitive to the angle of incidence.[33] Due to this intrinsic limitation of F-P-type cavities, such structural colors fabricated on flexible substrates tend to change when the substrates are bent or twisted out of shape, which significantly restricts their applications in the field of flexible optoelectronics. Recently, asymmetric F-P-type cavities have been proposed to realize reflective color filtering,[28,29] the total thickness of the top semi-transparent layer and the middle dielectric spacer in these devices is generally above 100 nm, which may limit their minimum pixel size to above 500 nm, i.e. on the order of the visible light wavelength. In addition, these demonstrations[28,29] together with many previous plasmonics color printing devices[6,7,10,13] all rely on the use of either reflected light or scattered light to generate a RGB-based color system, whose reflectivity is well known to be relatively lower than subtractive colors in the CMY color system for the application in emissive displays.[34] Finally, it is noteworthy that the reflection based structural colors often have a broad full width at half maximum (FWHM)[28], which essentially limits the achievable range of color gamut.

In this work, we propose an asymmetric ultrathin F-P-type lossy cavity to realize vivid subtractive flexible structural colors, exhibiting a deep-subwavelength resolution, a wide color gamut and a low sensitivity to the angle of incidence. We demonstrate an illustrative palette of such subtractive colors by simply changing the thickness of the top metal layer and the middle dielectric layer in the lossy F-P cavity, including the pigment color primaries: cyan, magenta, and yellow (CMY). The negligible light propagation phase shift in the ultrathin lossy layer leads to the incident-angle-invariant subtractive colors within the angle range of ±60°, and the ultrathin structural configuration also leads to a super-high spatial resolution. Moreover, the F-P-type lossy cavity can be easily fabricated by using standard thin-film deposition techniques such as electron-beam (e-beam) evaporation on either rigid or flexible substrates, thereby allowing for large-scale, low-cost implementation on practical devices of corrugated surfaces. To demonstrate these advantages associated with our new design, we experimentally realize (1) a two-dimensional sketched image of a Chinese ink-wash painting prawn with the proposed structure at a resolution well beyond the diffraction limit and (2) some flexible structural color membranes with wide color gamut and large viewing angle well adhered on an airplane model with complex surfaces.

2. Results and Discussion

2.1. Wide color gamut

As shown in **Figure 1**(a), our structural color system is an asymmetrical ultrathin F-P-type lossy cavity, consisting of a highly absorbing material - amorphous silicon (*a*-Si) dielectric film sandwiched between a top silver (Ag) film and a bottom aluminum (Al) film seated on a silicon (Si) substrate. The Al film functions as a reflective mirror while the ultrathin Ag film acts as a partially reflective mirror. Here, Si and Al are chosen because they are the most abundant materials on earth, and have been widely used in electronics industry for several decades. More importantly, Si reveals a strong absorption property at visible frequencies[35] and Al has a high reflectivity over all the visible wavelengths.[36] Ag is selected as the top-

layer material because of its lowest absorption loss and high reflectivity. In order to increase the adhesion and flatness of adjacent metal and Si layers, chromium (Cr) is deposited on the silicon substrate and on the *a*-Si layer, respectively. All these layers were deposited by using e-beam evaporation successively.

As shown in Figure 1(b), a palette of reflective subtractive colors can be easily obtained by simply changing the thickness of the Ag layer, h_1, and the thickness of the *a*-Si layer, h_2. Corresponding positions of these colors are plotted in the CIE 1931 color space, as shown in Figure 1(c), which confirms the capability for achieving the main colors in the CMY color system. Figure 1(d) presents the measured reflectance spectra for the samples with the *a*-Si layer thickness h_2 varied from 20 to 60 nm and the top Ag layer thickness h_1 fixed at 15 nm, where the spectral valleys redshift and the reflectance maxima are above 60%, leading to a high color brightness. The contour map of the experimental reflectance spectra plotted in Figure 1(e) further demonstrates the spectral dependence on h_2. In addition, Figure 1(f) shows the reflectance spectra of the samples with the top Ag layer thickness h_1 varied from 10 to 25 nm and the *a*-Si layer thickness h_2 fixed at 40 nm, also revealing a pronounced reflectance minimum intensity dependence on h_1 yet a weak reflectance valley shift. As a result, a wide color gamut with high color brightness is realized by jointly varying h_1 and h_2 of the asymmetric lossy cavity as demonstrated in Figure 1(b) and (c).

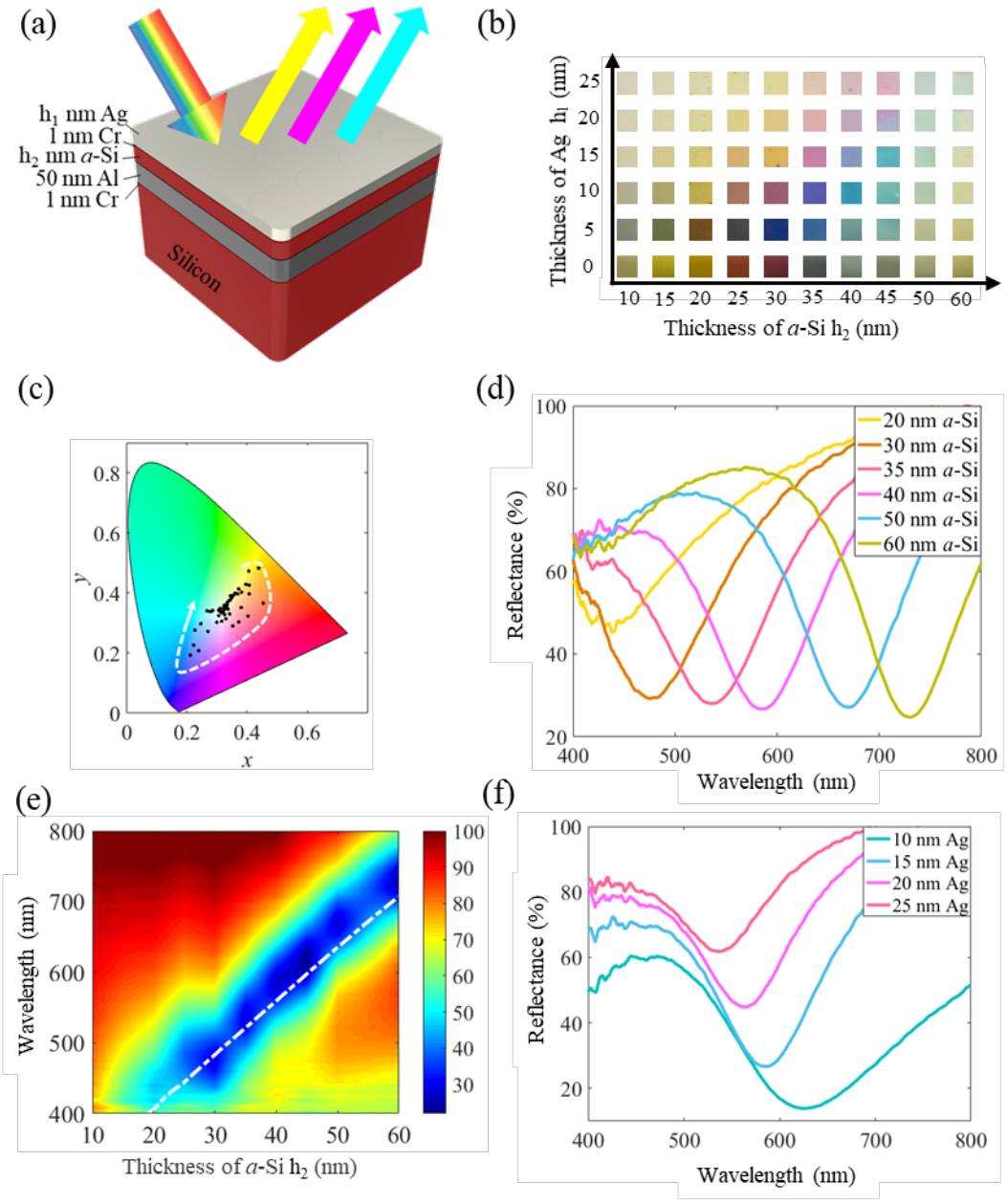

Figure 1. (a) Illustration of the proposed asymmetric F-P-type lossy cavity for realization of subtractive structural colors. (b) Recorded color palette of the reflective subtractive colors as functions of the thicknesses of the top Ag layer and the lossy medium layer in the cavity in (a). Each palette square has a size of 7 x 7 mm^2 and the whole array is under illumination by an unpolarized white light. (c) CIE1931 chromaticity diagram overlaid with the black points corresponding to the colors extracted from (b). (d) Measured reflectance spectra of six asymmetrical cavities with the lossy *a*-Si layer thickness varying from 20 to 60 nm. The thickness of the top Ag layer is kept constant as 15 nm. (e) Contour map of the experimental

reflectance spectra as functions of the incident wavelength and the *a*-Si layer thickness. The white dashed line outlines the valley positions calculated by the transfer matrix method (TMM) with the experimental structural parameters. (f) Measured reflectance spectra of four asymmetrical cavities with the top Ag layer thickness varying from 10 to 25 nm. The thickness of the lossy *a*-Si layer is kept constant as 40 nm. The reflectance spectra in (d) and (f) were measured using a 100x objective with a NA of 0.9.

2.2. Physical mechanism

In our color system, the top Ag layer is designed to be optically semi-transparent, allowing the incident light to penetrate into the *a*-Si layer and generate resonant absorption. The thickness of the top Ag layer mainly determines the reflectance valley intensity of each cavity while the *a*-Si spacer thickness mainly determines the reflectance valley position. The bottom metal layer and the silicon substrate are thick enough to prevent any light transmission. The reflectance of the asymmetric lossy cavity can be calculated as the coherent accumulation of the partial waves reflected from the F-P cavity as schematically shown in **Figure 2**(a). The total reflectance R of the cavity is given as $R=|r|^2$, and here the reflection coefficient r can be expressed as:

$$r = r_{12} + \frac{t_{12}t_{21}r_{23}}{e^{-2j\tilde{\beta}} - r_{21}r_{23}} \tag{1}$$

where $\tilde{\beta} = \frac{2\pi}{\lambda}\tilde{n}_2 h_2 \cos(\theta_2) = \beta + j\beta'$ is the accumulated one-way complex phase of the incident light in the *a*-Si layer (i.e. the same accumulated phase for the upward and downward waves $S_{\uparrow/\downarrow}$ in Figure 2(a)), with λ being the incident wavelength, $\tilde{n}_2 = n_2 + ik_2$ being the complex refractive index of the *a*-Si layer, and θ_2 being the angle of incidence in the *a*-Si layer. Here, the subscripts, 1, 2 and 3, represent the air above the Ag layer, the *a*-Si spacer, and the Al layer, respectively. Ideally, a reflective subtractive color will appear when the incident light satisfies the following phase condition:

$$\phi_{21} + 2\beta + \phi_{23} = 2\pi m \quad (2)$$

where ϕ_{21} and ϕ_{23} represent the phase shift of the reflection coefficients r_{21} and r_{23} at the Ag/*a*-Si interface and the Al/*a*-Si interface, and m is an integer. More details on the derivation of equations (1) and (2) can be found in the Experimental section.

The variation of reflectance valley position changes the color hue of the cavity, and the total reflection intensity determines the color brightness. From Equation 2, we could conclude that the most convenient way to tune the reflectance valley is to change the transmission phase by directly varying the thickness of the *a*-Si layer. Here, we get the reflective spectra calculated by the transfer matrix method (TMM)[37]. Figure 2(b) demonstrates that the varying *a*-Si thickness changes the reflectance valley position, which gives the similar results as shown in Figure 1(d) and (e).

However, a wide color gamut cannot be obtained by just changing the reflectance valley positions in the spectra, and another degree of freedom is needed to manipulate its brightness, i.e. the thickness of the Ag layer. Considering that the numerator of the second term in Equation (1) would always have an opposite sign to the first term[38] and the transmission of the Ag layer decreases when its thickness grows (the red lines in Figure 2(c)), which means the total reflection increases on this condition, further resulting in a greater brightness. At the same time, when we vary the thickness of the Ag layer, its reflection phase is also changed (the blue lines in Figure 2(c)), thus the resonant frequency represented by the valley position in the spectra is also tuned, as shown in Figure 2(d). Therefore, by combining the changing thicknesses of both the *a*-Si and Ag layers, a wide color gamut with tuning color and brightness can be realized.

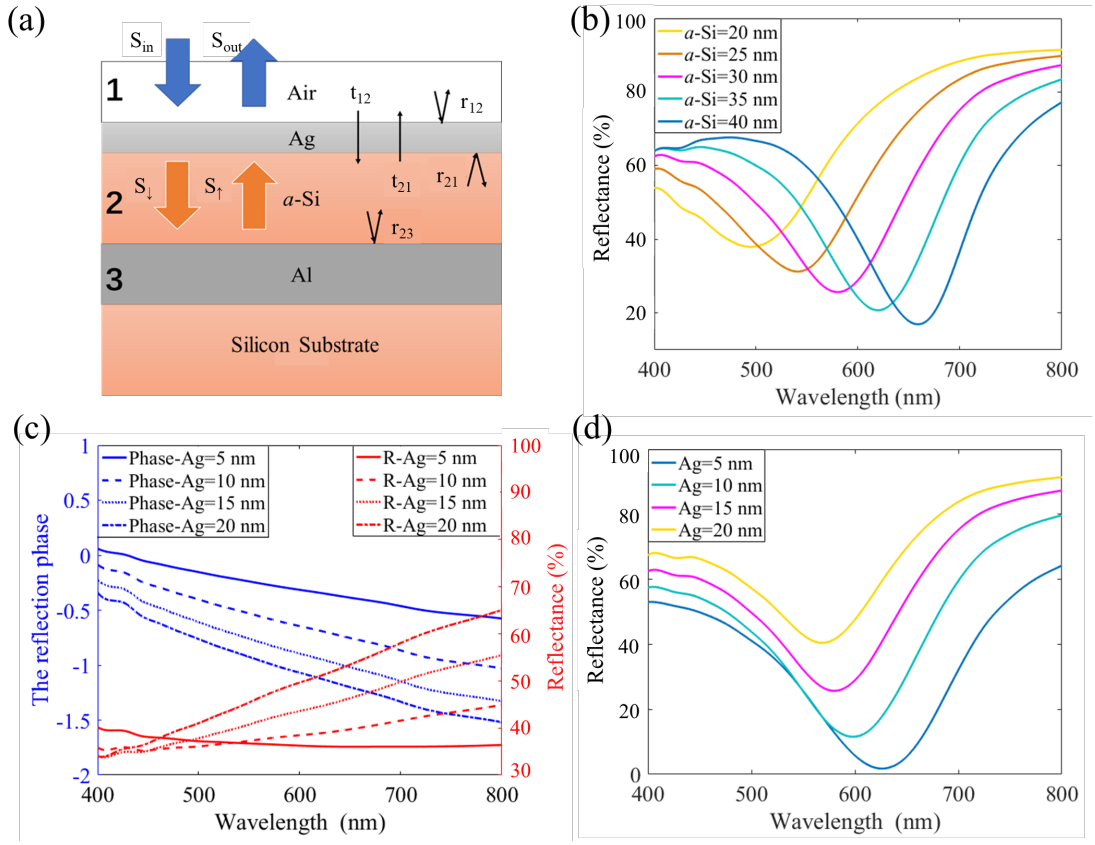

Figure 2. (a) Schematics of theoretical analysis. (b) Calculated reflectance spectra by the TMM method at normal incidence for the cavities with the *a*-Si layer thickness varying from 20 to 40 nm. The thickness of the Ag layer is fixed at 15 nm. (c) The reflection phase and reflectance for the Ag thickness with 5, 10, 15, 20 nm calculated by the TMM method. (d) The reflective spectra calculated by the TMM method at normal incidence for the cavities with the thickness of the Ag layer varying from 5 to 20 nm. The thickness of the *a*-Si layer is fixed at 30 nm.

2.3. Wide viewing angle

Due to the negligible propagation phase shift in the ultrathin *a*-Si layer, the asymmetric F-P-type structural colors exhibit excellent angle independence up to ±60° that is addressing a crucial challenge for current optical filters. The simulated results for both *p*-polarization and *s*-polarization are shown in **Figure 3**(a) and (b), respectively, which seem in excellent agreement with the experimental observations in Figure 3(c).

The physical mechanism of the angular independence: According to Equation (2), if the propagation phase shift and reflection phase shift accumulated by the proposed structure keep invariable for the changing angle of incidence, the reflectance spectra will remain the same. As the thickness of the *a*-Si layer is much thinner compared to the wavelength of incident light, thus the induced phase shift is negligible. In addition, the high refractive index of *a*-Si can also behave a vital role. The phase shift of the resonant wavelength at an incident angle θ_i is found to be $\frac{\partial \lambda_0}{\partial \theta_i} \propto \frac{\sin\theta_i \cos\theta_i}{n_2^2 - \sin\theta_i^2}$. Obviously, a larger refractive index n_2 will result in a smaller phase shift, confirming that the angular tolerance is enhanced by the high refractive index n_2 of *a*-Si in the cavity.[39]

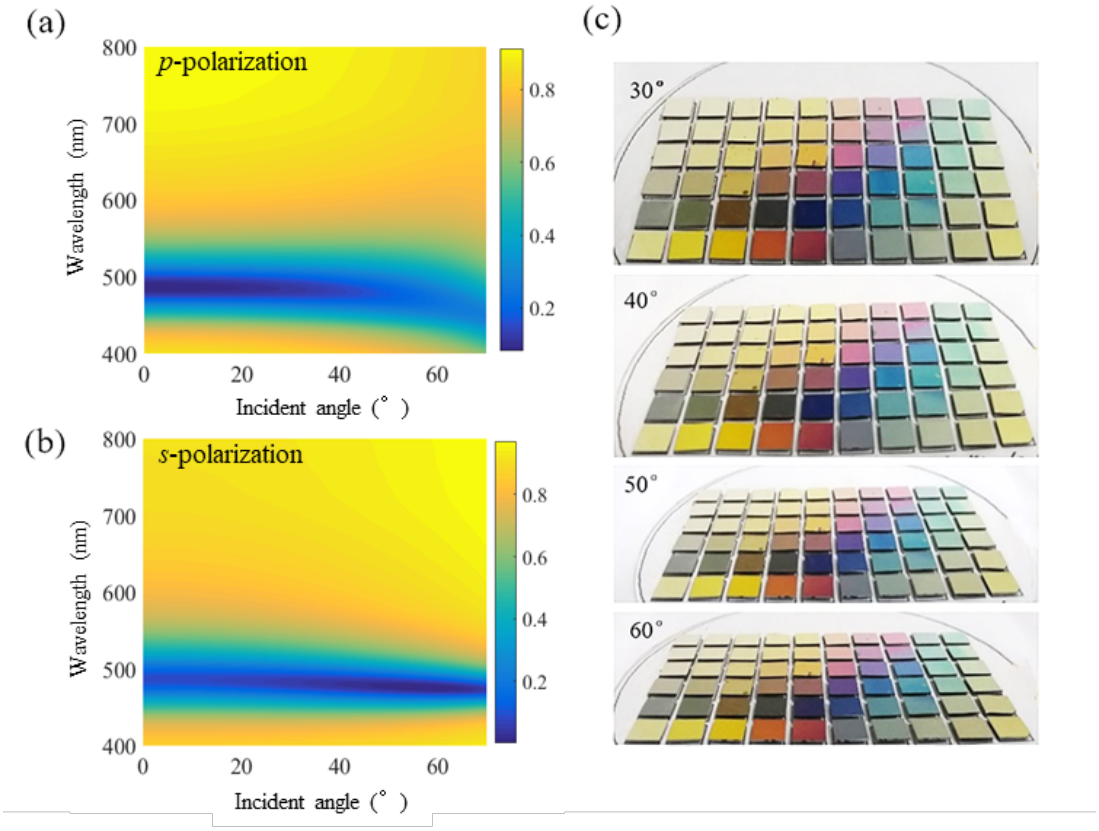

Figure 3. Contour map of the simulated angle-resolved reflectance spectra for the lossy F-P cavity with h_1 = 15 nm and h_2 = 30 nm under (a) *p*-polarized and (b) *s*-polarized illumination. (c) Recorded photographs of the correspondingly practical color palette taken under the outdoor ambient light with an oblique incidence of 30°, 40°, 50°, 60°, respectively.

2.4. Sketched printing with deep-subwavelength spatial resolution

The two-dimensional sketched image of the Chinese ink-wash painting prawn (**Figure 4**(a)) with the size of 50 μm × 53 μm was printed by the electron beam lithography (EBL) and e-beam evaporation. After generating the prawn pattern by EBL, 1 nm Cr, 50 nm Al, 35 nm *a*-Si, 1 nm Cr and 14 nm Ag were evaporated sequentially by the e-beam evaporation process. Figure 4(b) depicts the ultimately obtained reflection-mode optical microscope image, illuminated by an un-polarized white light. Figure 4(c) shows the SEM image of the region outlined in Figure 4(a), and Figure 4(d) shows the enlarged view of the regions outlined in Figure 4(c). Bright and distinct colors are observed, even at the feelers and legs of the prawn, which demonstrates that this printing scheme has a high resolution. The high resolution of this structural color is due to the ultrathin thickness of this cavity, where the total thickness of the top semi-transparent layer and the middle dielectric spacer in these devices is less than 85 nm. As shown in Figure 4(d), the minimum size of the feelers is 160 nm, beyond the diffraction limit of visible light (~250nm). Therefore, the estimated dots per inch (dpi) reach to almost 150,000 in the geometrical space, a higher resolution than the Lena image previously reported.[12] One example was given to further prove the feasibility of this structure for high-resolution sketched printing. Figure 4(e) shows a reflection-mode optical microscope image of the sketched nanoprinting Chinese poetry with size of 600 μm × 200 μm, and the Chinese characters can be clearly displayed. As shown in Figure 4(f) and (g), the curved hook under nanometer scale can be seen clearly. Furthermore, it only takes about 90s for the EBL to fabricate this complicated poetry with about 120 Chinese characters, which is high-efficient and can be used for high-density optical data storage conveniently.

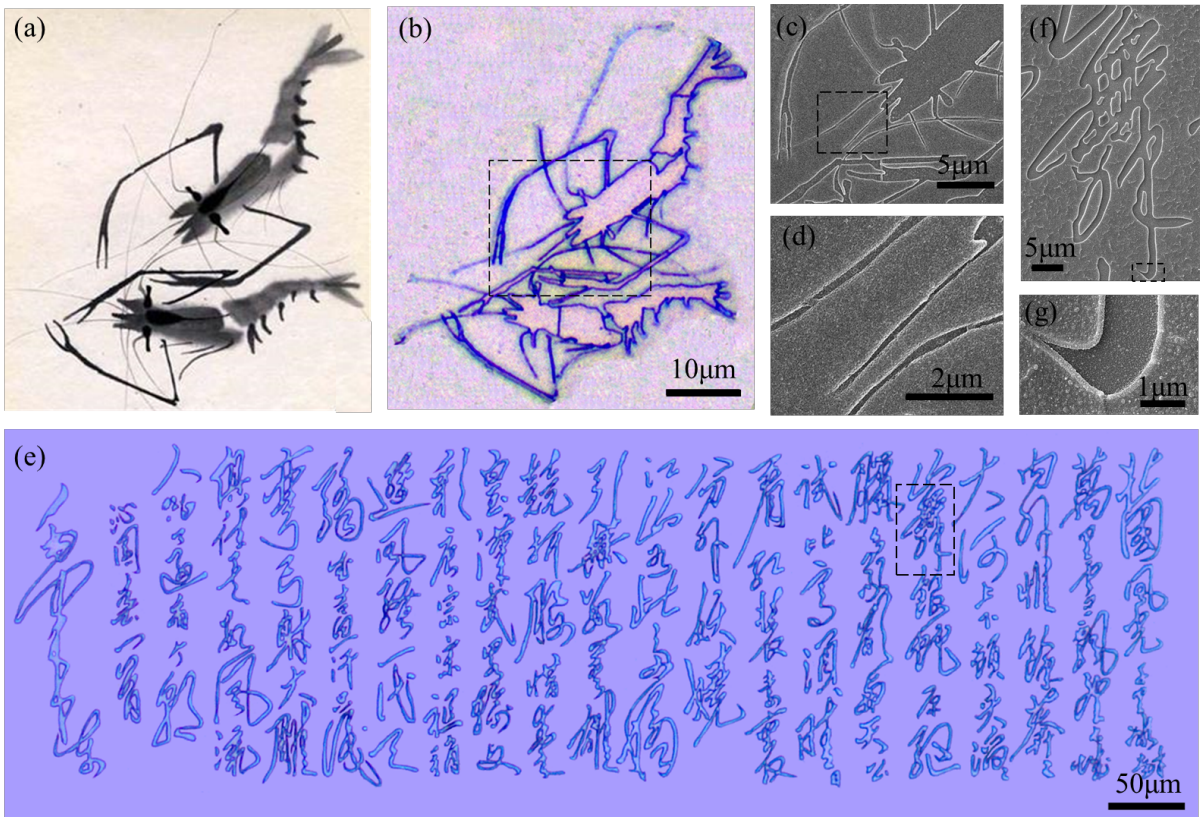

Figure 4. (a) Optical image of a Chinese ink-wash painting prawn and (b) its high-resolution nano-printing image (50 μm × 53 μm) by employing the asymmetric F-P-type lossy cavity. (c) SEM image of the region outlined in (b), and (d) an enlarged view of the region outlined in (c). (e) Optical image of a sketched nano-painting Chinese poetry (600 μm × 200 μm) made with the asymmetric F-P-type lossy cavity under illumination by an un-polarized white light. (f) SEM image of the region outlined in (e), and (g) an enlarged view of the region outlined in (f).

2.5. Structural color on flexible substrate

Flexible structural colors attract extensive interests in flexible optoelectronic engineering owing to their high flexibility and foldability. Here, we evaporated the multilayer films on the flexible aluminum foil as the substrate to get the flexible color membranes. As shown in **Figure 5**, the flexible structural color samples with different colors are perfectly adhered on the curved surfaces of the three-dimensional airplane model, which demonstrates that the flexible structural color can be used as the smart skin for camouflage or visible stealth. Due to the angular insensitivity, the property of the flexible structural color remains nearly

unchanged when the color membranes are bent, or twisted. As for the mature semiconductor or microelectromechanical systems (MEMS) technology, other flexible substrates can all be utilized, including the polyimide (PI), polyethylene terephthalate (PET), polydimethylsiloxane (PDMS), silicone, to just name a few. Furthermore, the fabrication technique of the flexible version of our color system is compatible with current micro-/nanofabrication industrial methods and has the potential for large-scale production.

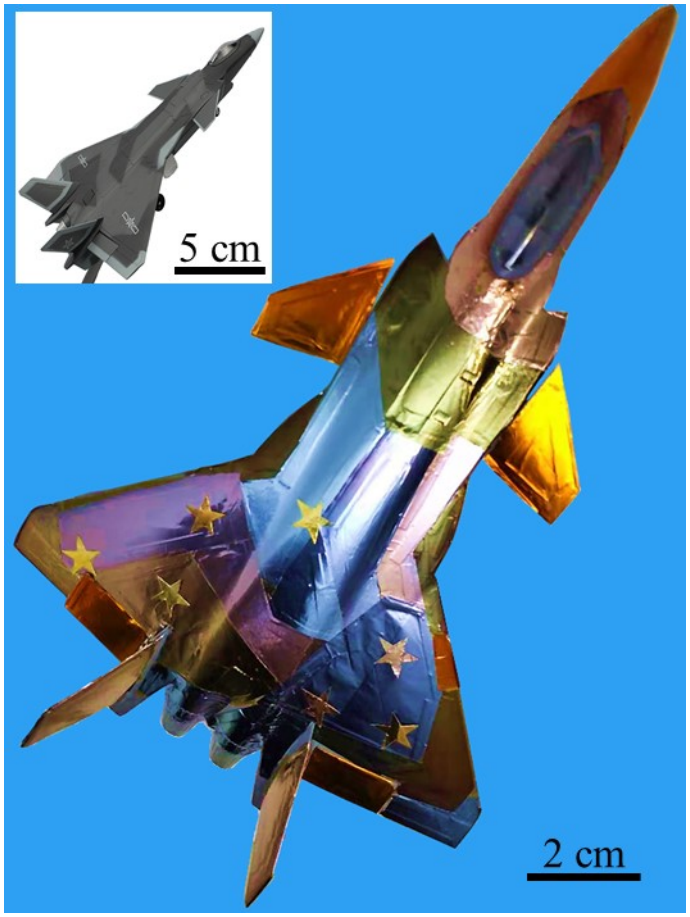

Figure 5. Photograph of a three-dimensional airplane model coated with flexible structural color membranes. The inset shows the original model.

3. Conclusion

In conclusion, a subtractive structural color with a deep-subwavelength resolution generated by an ultrathin asymmetric F-P-type lossy cavity is proposed to realize wide color gamut, large viewing angle and good flexibility. By simply changing the thickness of the middle *a*-Si

lossy layer and the top Ag mirror layer, the demonstrated structural color can span the whole CMY color system. The ultrathin lossy *a*-Si layer induces a negligible propagating phase change, giving rise to an extraordinary angular tolerance of up to ±60°, and also leads the structural color to get a high resolution. The high resolution enables the printing of a two-dimensional sketched image of a complicated Chinese ink-wash painting prawn with a pixel density up to 150,000 dpi, and the broadened color gamut and enlarged viewing angle jointly enable the production of some flexible color membranes adhered well on a three-dimensional airplane model. The asymmetric F-P-type high-resolution structural color proposed here will be greatly attractive for diverse applications, covering high-definition displays, high-resolution color filters, high-density optical data storage, as well as flexible optoelectronic components used for smart wrist watch, smart bracelet, camouflage coating or other wearable devices.

4. Experimental Section

Sample fabrication: The bottom aluminum (Al) layer of 50 nm, the middle amorphous silicon (*a*-Si) layer and the top sliver (Ag) layer were deposited by the electron-beam (e-beam) evaporation on a silicon (or flexible aluminum foil) substrate at a rate of 2 $Å s^{-1}$ for Al, 1 $Å s^{-1}$ for *a*-Si and 0.5 $Å s^{-1}$ for Ag with a vacuum pressure less than 4×10^{-4} Pa at 25 °C. The two-dimensional image of the Chinese ink-wash painting prawn was printed by the electron beam lithography (EBL) and e-beam evaporation. The e-beam photoresist, Poly(methyl methacrylate) (PMMA) (formulated as product number RE300.20.5), was spin-coated onto silicon substrate to a thickness of 195 nm at the rate of 3000 rpm for 30 s, followed by tempering 2 min on the hot plate at 180 °C. EBL was performed using NanoBeam Limitd nB5 EBL system with an accelerating voltage of 100 kV and a beam current of 100 pA. The dose used for the structure was 5.6 $C m^{-2}$. The development process was used by developing the sample in methyl isobutyl ketone (MIBK) solution at 25°C for 2 min, followed by rinsing in

isopropyl alcohol (IPA) for 2 min. Finally, the sample was blow-dried under a steady stream of N_2. And then, 1 nm Cr, 50 nm Al, 35 nm *a*-Si, 1 nm Cr and 14 nm Ag were deposited by e-beam evaporation process, sequentially. The Chinese poetry was nano-printed following the above process. After obtaining the pattern, 1 nm Cr, 50 nm Al, 32 nm *a*-Si, 1 nm Cr and 16 nm Ag were deposited by e-beam evaporation process, sequentially.

Optical measurement. The reflectance of the prepared F-P-type lossy cavities were measured using a NOVA-EX spectrometer coupled to a microscope system (Olympus-BX53). A white light source in the wavelength from 400 to 800 nm was focused by an objective onto the sample surface and the reflected light was collected by the same objective (MPlanFLN, NA = 0.9, 100x).

Theoretical analysis. As shown in Figure 2(a) in the main text, we set the air above the Ag layer and the *a*-Si layer as the region 1 and 2, respectively, and the transmission and reflection coefficients of the Ag layer can be expressed as $t_{12/21}$ and $r_{12/21}$, respectively. The Al layer is marked as region 3 and its reflection coefficient is represented as r_{23}. Both coefficients *t* and *r* can be calculated by the TMM method. By setting the input/output waves at the air region as $S_{\text{in/out}}$, and the upward and downward waves in the *a*-Si spacer as $S_{\uparrow/\downarrow}$, and applying corresponding boundary conditions at the Al/*a*-Si, Ag/*a*-Si and air/Ag interfaces, we can obtain the following set of equations,

$$\begin{cases} S_{\uparrow} = r_{23} e^{2i\tilde{\beta}} S_{\downarrow} \\ r_{21} S_{\uparrow} + t_{12} S_{in} = S_{\downarrow} \\ S_{out} = r_{12} S_{in} + t_{12} S_{\uparrow} \end{cases} \tag{3}$$

where $\tilde{\beta}$ is as defined in the main text. By solving this set of equations and defining $S_{\text{out}} = rS_{\text{in}}$, we can obtain Equation (1) in the main text. In the meanwhile, the amplitudes of the waves in the *a*-Si layer are given as

$$\begin{cases} S_{\downarrow} = \dfrac{t_{12}S_{in}}{1-r_{21}r_{23}e^{2i\tilde{\beta}}} \\ S_{\uparrow} = \dfrac{t_{12}r_{23}e^{2i\tilde{\beta}}S_{in}}{1-r_{21}r_{23}e^{2i\tilde{\beta}}} \end{cases} \tag{4}$$

Assuming the absorption of the cavity mainly comes from the *a*-Si layer, we can calculate the total absorption by the two wave amplitudes in this layer as

$$A \propto \left|S_{\downarrow}\right|^2 + \left|S_{\uparrow}\right|^2 \propto \left|\frac{t_{12}}{1-r_{21}r_{23}e^{2i\tilde{\beta}}}\right|^2 \tag{5}$$

Since the real part of $\tilde{\beta}$ is much larger than its imaginary part, attributing to a much larger real part of the refractive index of the *a*-Si material compared to its imaginary part, and also $\left|r_{21}r_{23}\right|$ varies very slowly with the wavelength, we can assume $\left|r_{21}r_{23}e^{2i\tilde{\beta}}\right|$ to be nearly constant. Therefore, the key parameter determining the maximum absorption wavelength is the phase of $r_{21}r_{23}e^{2i\tilde{\beta}}$, which occurs at the phase equals to $2m\pi$ with m being an integer as described in Equation (2) in the main text.

Numerical simulation. The reflectance spectra of the studied asymmetric F-P-type lossy cavities were calculated using the transfer matrix method (TMM). The complex refractive index of *a*-Si used in the calculations was measured by a spectroscopic ellipsometer, with results shown in **Figure 6**. The complex refractive indices of Al and Ag used in the calculation were obtained from the Palik data in the material library.

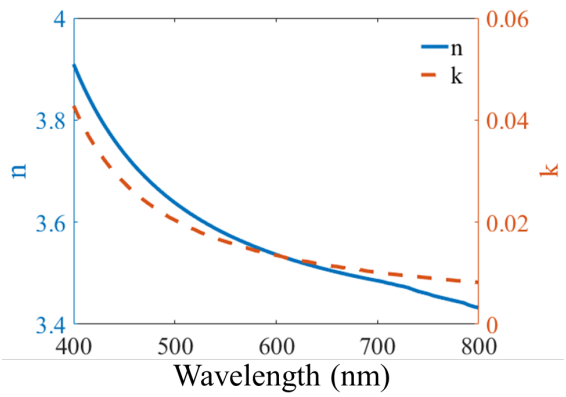

Figure 6. The measured complex refractive index (*n*, *k*) of *a*-Si.

Acknowledgements

Jiancun Zhao and Meng Qiu contributed equally to this work. The work was financially supported by the National Natural Science Foundation of China (51622509), the Strategic Initiative Project, the 111 Project (B13044), and the Innovation Foundation for Doctor Dissertation of Northwestern Polytechnical University (CX201830). The authors would also like to thank the Analytical & Testing Center of Northwestern Polytechnical University for the EBL fabrication.

References

[1] S. Yokogawa, S. P. Burgos, H. A. Atwater, *Nano Lett.* **2012**, *12*, 4349.

[2] Y.-W. Huang, W. T. Chen, W. -Y. Tsai, P. C. Wu, C. -M. Wang, G. Sun, D. P. Tsai, *Nano Lett.* **2015**, *15*, 3122.

[3] Y. Cui, R. S. Hegde, I. Y Phang, H. K. Leeac, X. Y. Ling, *Nanoscale* **2014**, *6*, 282.

[4] T. W. Ebbesen, H. J. Lezec, H. F. Ghaemi, T. Thio, P. A Wolff, *Nature* **1998**, *391*, 667.

[5] E. Heydari, J. R. Sperling, S. L. Neale, A. W. Clark, *Adv. Funct. Mater.* **2017**, *27,* 1701866.

[6] D. Inoue, A. Miura, T. Nomura, H. Fujikawa, K. Sato, N. Ikeda, D. Tsuya, Y. Sugimoto, Y. Koide, *Appl. Phys. Lett.* **2011**, *98*, 093113.

[7] G. Si, Y. Zhao, H. Liu, S. Teo, M. Zhang, T. J. Huang, A. J. Danner, J. Teng, *Appl. Phys. Lett.* **2011**, *99*, 033105.

[8] Y. S. Do, J. H. Park, B. Y. Hwang, S. -M. Lee, B. -K. Ju, K. C. Choi, *Adv. Opt. Mater.* **2013**, *1*, 133.

[9] J. Xue, Z. –K. Zhou, Z. Wei, R. Su, J. Lai, J. Li, C. Li, T. Zhang, X. -H. Wang, *Nat. Commun.* **2015**, *6*, 8906.

[10] J. Zhao, B. Gao, H. Li, X. Yu, X. Yang, Y. Yu, *J. Nanophoton.* **2017**, *11*, 036020.

[11] M. Miyata, H. Hatada, J. Takahara, *Nano Lett.* **2016**, *16*, 3166.

[12] K. Kumar, H. Duan, R. S. Hegde, S. C. W. Kohl, J. N. Wei, J. K. W. Yang, *Nat. Nanotechnol.* **2012**, *7*, 557.

[13] G. Si, Y. Zhao, J. Lv, M. Lu; F. Wang, H. Liu N. , Xiang, T. J. Huang, A. J. Danner, J. Teng, Y. J. Liu, *Nanoscale* **2013**, *5*, 6243.

[14] V. R. Shrestha, S. -S. Lee, E. -S. Kim, D. -Y. Choi, *Nano Lett.* **2014**, *14*, 6672.

[15] A. S. Roberts, A. Pors, O. Albrektsen, S. I. Bozhevolnyi, *Nano Lett.* **2014**, *14*, 783.

[16] J. Zhao, X. Yu, X. Yang, Q. Xiang, H. Duan, Y. Yu, *Opt. Express* **2017**, *25*, 23137.

[17] B. -R. Lu, C. Xu, J. Liao, J. Liu, Y. Chen, *Opt. Lett.* **2016**, *41*, 1400.

[18] T. D. James, P. Mulvaney, A. Roberts, *Nano Lett.* **2016**, *16*, 3817.

[19] R. Mudachathi, T. Tanaka, *Sci. Rep*. **2017**, *7*, 1199.

[20] J. Zhao, X. Yu, X. Yang, C. A. Tee, W. Yuan, Y. Yu, *Opt. Lett.* **2019**, *44*, 963.

[21] M. A. Schmidt, D. Y. Lei, L. Wondraczek, V. Nazabal, S. A. Maier, *Nat. Commun.* **2012**, *3*, 1108.

[22] Y. Zhang, Q. Zhang, X. Ouyang, D. Y. Lei, A. P. Zhang, H.-Y. Tam, *ACS Nano* **2018**, *12*, 9913.

[23] B. Zeng, Y. Gao, F. J. Bartoli, *Sci. Rep*. **2013**, *3*, 2840.

[24] A. F. Kaplan, T. Xu, L. J. Guo, *Appl. Phys. Lett.* **2011**, *99*, 143111.

[25] Y. -K. R. Wu, A. E. Hollowell, C. Zhang, L. J. Guo, *Sci. Rep*. **2013**, *3*, 1194.

[26] Y. Zhao, Z. Xie, H. Gu, C. Zhu, Z. Gu, *Chem. Soc. Rev*. **2012**, *41*, 3297.

[27] F. Liu, B. Dong, X. Liu, Y. Zheng, J. Zi, *Opt. Express* **2009**, *17*, 16183.

[28] Z. Yang, Y. Zhou, Y. Chen, Y. Wang, P. Dai, Z. Zhang, H. Duan, *Adv. Opt. Mater.* **2016**, *4*, 1196.

[29] C. Yang, W. Shen, Y. Zhang, K. Li, X. Fang, X. Zhang, X. Liu, *Sci. Rep.* **2015** , *5* , 9285.

[30] Z. Li, S. Butun, K. Aydin, *ACS Photonics* **2015**, *2*, 183.

[31] Z. Yang, Y. Chen, Y. Zhou, Y. Wang, P. Dai, X. Zhu, H. Duan, *Adv. Opt. Mater.* **2017**, *5*, 1700029.

[32] Y. Chen, X. Duan, M. Matuschek, Y. Zhou, F. Neubrech, H. Duan, N. Liu, *Nano Lett*, **2017**, *17*, 5555.

[33] W. Yue, S.-S. Lee, E.-S. Kim, *Opt. Express* **2016**, *24*, 17115.

[34] K. Xiong, D. Tordera, M. P Jonsson, A. B Dahlin, *Rep. Prog. Phys.* **2019**, *82*, 024501.

[35] S. S. Mirshafieyan, J. Guo, *Opt. Express* **2014**, *22*, 31545.

[36] C. Yang, W. Shen, Y. Zhang, K. Li, X. Fang, X. Zhang, X. Liu, *Sci. Rep*. **2015**, *5*, 9285.

[37] L. Zhou, Z. Song, X. Huang, C. T. Chan, *Nanophotonics* **2012**, *1*, 181.

[38] S. Fan, W. SuhFan, *J. Opt. Soc. Am. A* **2003**, *20*, 569.

[39] K. -T. Lee, C. Ji, L. J. Guo, *Appl. Phys. Lett.* **2016**, *108*, 031107.